Journal of Ceramic Processing Research. Vol. 25, No. 5, pp. 776~785 (2024)
(Received 1 July 2024, Received in revised form 9 September 2024, Accepted 11 September 2024)
https://doi.org/10.36410/jcpr.2024.25.5.776

J O U R N A L O F
Ceramic Processing Research

Preparation and aging properties of $BiFe_{1-x}Al_xO_3$ ferroelectric thin films

Pang Hui[a,c], He Jingxian[b], Kong Qingfeng[c] and Zhang Fengqing[b,*]
[a]*Shandong University of Traditional Chinese Medicine, Jinan, 250399, Shandong, China*
[b]*Shandong Jianzhu University, Jinan, 250101, Shandong, China*
[c]*Jining No.1 People's Hospital, Jining, 272002, Shandong, China*

Thin films of $BiFe_{1-x}Al_xO_3$ (BFAlO, x=0-0.03) were fabricated on ITO-coated glass substrates using the sol-gel technique. Comprehensive analyses conducted through X-ray diffraction (XRD), scanning electron microscopy (SEM), and Raman spectroscopy confirmed that all BFAlO thin film samples consist of both R3c and Pnma phases. The incorporation of Al was found to refine the grain size, markedly enhancing the density of the BFAlO thin film samples. X-ray photoelectron spectroscopy (XPS) analysis revealed that at an Al doping level of 0.02, there was a substantial reduction in the concentration of oxygen vacancies and Fe^{2+} ions within the films. These BFAlO thin film samples demonstrated a robust remnant polarization strength (2Pr=132.94 μC/cm²) and a lower coercive field strength (2Ec=690.52 kV/cm) when subjected to an applied electric field of 640 kV/cm. Additionally, after an aging period of 75 days, the samples showed commendable resistance to aging. The findings suggest that a moderate level of Al doping can significantly improve the ferroelectric stability of BFO films and bolster their resistance to the aging process.

Keywords: $BiFeO_3$, Al doping, Ferroelectric properties, Aging.

Introduction

$BiFeO_3$ (BFO) is a unique single-phase multiferroic material that possesses both ferroelectricity and ferromagnetism under ambient temperatures. The distinctiveness of BFO lies in its R3c space group and distorted perovskite structure, which endow BFO with a range of special physical properties [1, 2]. Specifically, the ferroelectricity in BFO originates from the *6s* lone pair electrons, while its G-type antiferromagnetism is attributed to the antiparallel spins of *d* electrons from adjacent Fe atoms [3]. Additionally, the spin spiral structure within the sublattice also contributes to its antiferromagnetic properties. BFO exhibits a high ferroelectric Curie temperature of up to 825 °C and an antiferromagnetic Néel temperature of 370 °C. It also possesses numerous advantages such as a large polarization strength, high transition temperature, and a narrow band gap [4]. Consequently, BFO holds significant potential for applications in multiferroic devices including sensors, magnetoelectric memories, and ferroelectric photovoltaics. Nonetheless, this approach encounters specific challenges, notably Bi's volatility at elevated temperatures, resulting in oxygen vacancy creation [5]. These issues can result in an increased leakage current density, thereby affecting the performances of BFO. Furthermore, the valence alternation between Fe^{3+} and Fe^{2+} can induce electronic transitions, which further exacerbate the issue of leakage current [6].

To enhance the performance of BFO thin films, researchers have explored various approaches, including the formation of heterostructures, the construction of multicomponent composite systems, optimization of fabrication processes, and doping modifications. Ma et al. [7] explored different annealing atmospheres influence the characteristics of the $BiFe_{0.91}Zr_{0.09}O_3$ thin films. Compared to the samples fabricated in air and N_2, those annealed in atmosphere of O_2 exhibited a lower leakage current density and a larger remnant polarization strength (2Pr = 70.26 μC/cm^2). He et al. [8] successfully fabricated xBIT-(1-x)BFMO thin films by adjusting the solid solution ratio. With a declining composite ratio of BIT ($Bi_4Ti_3O_{12}$) to BFMO ($BiFe_{0.98}Mn_{0.02}O_3$), the films experienced a phase shift from Fmm2 to R3c. Furthermore, doping modification is a validated strategy for enhancing BFO's structure and characteristics, particularly by introducing dopants at the A-site, B-site, or simultaneously at both sites. Wrzesińska and his colleagues studied the rare earth (RE = La, Eu, and Er) element doping in $Bi_{0.9}RE_{0.1}FeO_3$ thin films [9]. The research revealed that all of the $Bi_{0.9}RE_{0.1}FeO_3$ films exhibited enhanced magnetization, with the BLaFO sample achieving the highest saturation magnetization of 5.161 emu/g at 300 K. Zulkafli et al. [10] produced Al-doped BFO thin films, revealing that Al doping markedly narrowed the energy bandgap, with Al3p

*Corresponding author:
Tel : +86053186367285
Fax: +86053186367285
E-mail: zhangfengqing615@163.com

states present in both the valence and conduction bands. However, there is relatively less research on the effects of Al doping on the ferroelectric and aging properties of BFO thin films.

Due to the relatively small difference in ionic radii between Fe^{3+} (0.645 Å) and Al^{3+} (0.535 Å), and the fact that Al ions are less prone to valence changes, substituting Al for Fe can reduce the relative content of oxygen vacancies in BFO thin films. Additionally, Al doping will induce lattice distortion, which in turn has the potential to enhance the ferroelectric properties of BFO films. Consequently, the present study fabricated $BiFe_{1-x}Al_xO_3$ thin films with x values of 0, 0.01, 0.02, and 0.03, and conducted a detailed analysis of how Al doping altered the microstructure, electrical behavior, and long-term stability of these films.

Experimental

The BFAlO thin film samples were prepared by sol-gel method by accurately weighing all the necessary chemicals using the electronic balance, by dissolving $Bi(NO_3)_3$-$5H_2O$ in a solvent mixture of $(CH_2OH)_2$ and CH_3COOH in a ratio of 1:3, followed by sequential addition of $Fe(NO_3)_3 \cdot 9H_2O$ and $Al(NO_3)_3 \cdot 9H_2O$ and continuous stirring to ensure sufficient dissolution, followed by the addition of acetylacetone as a complexing agent, after stirring to obtain a 0.3 mol/L precursor solution, which was allowed to stand at room temperature for 24 hours to be set aside. The BFAlO precursor solution was dripped onto the ITO conductive glass, which was spin-coated in a homogenizer to form a wet film, and then quickly placed on a heating plate for pyrolysis, with the purpose of volatilization of organic solvents, and then placed the pyrolyzed BFAlO film into a rapid annealing furnace for annealing treatment, repeated the above steps, the BFAlO film samples of the desired thickness were finally prepared.

To test the film properties, the film samples were subjected to crystal structure analysis and physical phase identification using a D8-Advance model XRD. Raman testing of the BFAlO thin films was carried out using a SEED3000 Raman monitoring system with the aim of revealing the phase distribution and chemical structure characterization of the films. The elemental composition and chemical valence states of the thin film samples were determined using an XPS (Escalab 250Xi). In order to evaluate the ferroelectric properties of the films, the BFAlO thin films were tested for ferroelectric properties using a Multiferroic (Radiant, USA) ferroelectric tester. The surface microstructure of the samples were observed and the section thickness was measured using a scanning electron microscope (Apreo SEM); the measurement of the forbidden bandwidth of the thin film samples was measured using a UV-visible spectrophotometer (U-4100 Hitachi).

Results and Discussion

Fig. 1(a) presents the XRD patterns of BFAlO thin films at room temperature. All sample diffraction peaks match the standard spectrum of BFO (JCPDS: 86-1518) without any detectable impurity phases, confirming their Pseudoperovskite structure. Fig. 1(b) presents an enlarged view of the (104)/(110) planes, illustrating that as the Al doping concentration incrementally rises. There is a noticeable shift of the (104)/(110) diffraction peaks towards higher angles, indicative of an expanding lattice constant. This occurrence is likely due to the substitution of some Fe^{3+} ions (radius of 0.645 Å) in the BFO lattice with smaller Al^{3+} ions (radius of 0.535 Å), leading to lattice distortion and indicating successful doping [11]. Additionally, the merging of the (104) and (110) peaks into a broad peak is observed, suggesting a possible structural change in the BFAlO thin films [12].

To assess the stability of ABO_3 perovskite structure, the Goldschmidt tolerance factor (t) is introduced [13]. The calculation formula for the tolerance factor is as follows:

$$t = \frac{r_A + r_0}{\sqrt{2}(r_B + r_O)} \quad (1)$$

In BFAlO thin films, the ionic radius of Bi ions, Fe and Al ions, and O ions are denoted as r_A, r_B, and r_O, respectively. The t values for the thin film samples are calculated, which are 0.8886, 0.8891, 0.8896, and 0.8901, respectively. With the increase in the substitution amount of Al, the t exhibits an increasing trend, resulting in the stretching and tilting of the FeO_6 octahedra. This results in a progressive shift of the crystal structure from the R3c phase to the orthorhombic Pmna phase [14].

Fig. 2(a)-(d) present the SEM images of BFAlO thin film samples with varying Al doping concentrations. The undoped BFO thin film sample displays increased grain sizes, a non-uniform distribution, a coarse texture, and some porosity, likely due to organic solvent evaporation

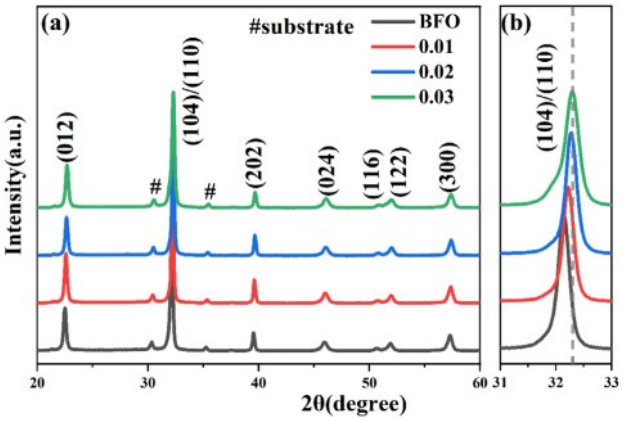

Fig. 1. (a) XRD pattern of the BFAlO thin films with different Al content, (b) Local amplification of 31°-33°.

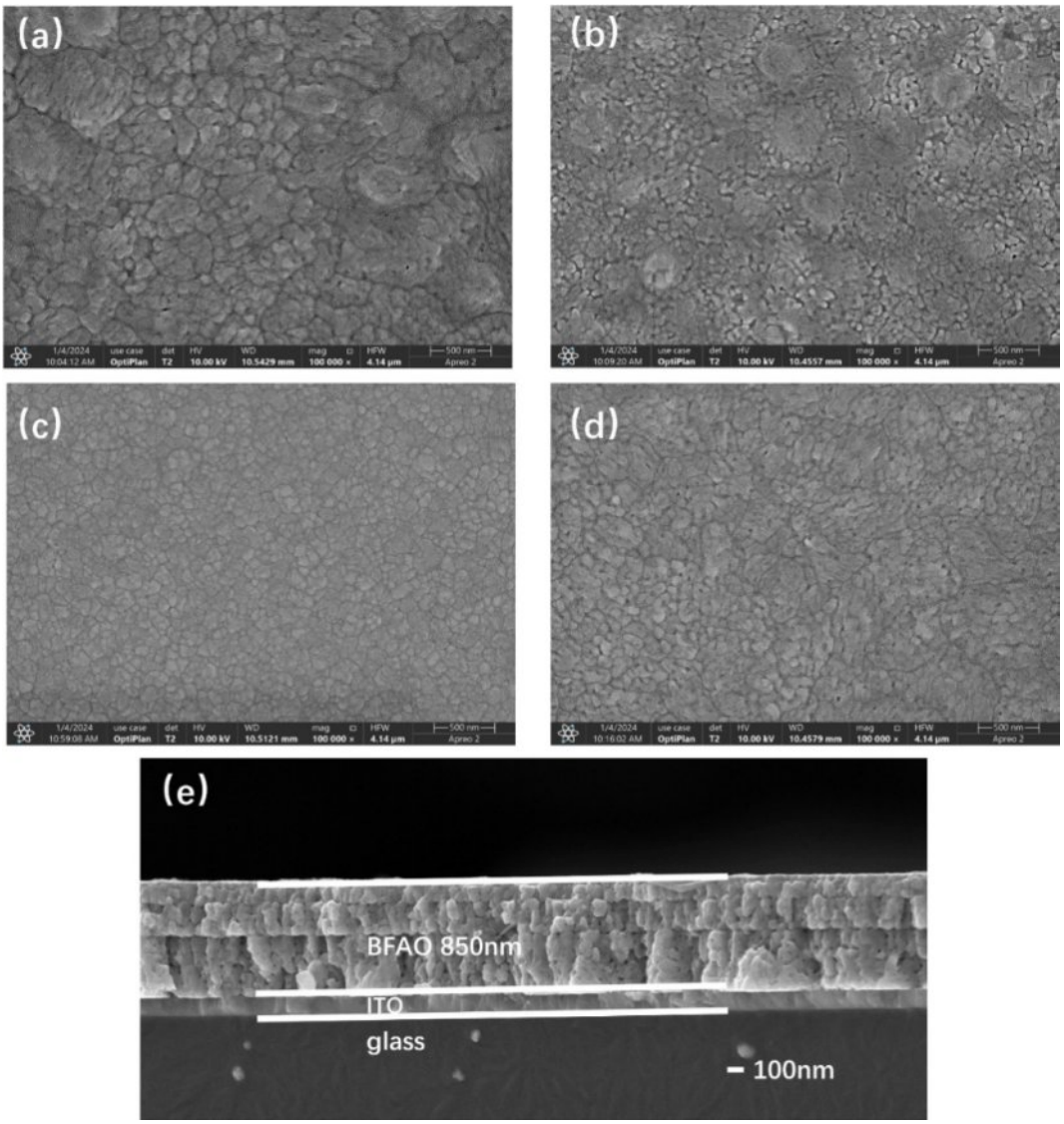

Fig. 2. SEM surface morphology images of the BFAlO films with different Al content, (a) BFO, (b) $BF_{0.99}Al_{0.01}O$, (c) $BF_{0.98}Al_{0.02}O$, (d) $BF_{0.97}Al_{0.03}O$, (e) Cross-section morphology of the BFAlO film with 0.02 doping level.

during production [15]. The average grain size of the films doped with Al shows a significant reduction, indicating that Al doping can refine the grain size. This effect is likely due to the Kirkendall effect, caused by the different diffusion rates of metal atoms [16, 17]. When the doping level is 0.02, the BFAlO thin film sample has smaller average grain size and a more dense and uniform surface. With further increase in doping level, the grain size of the BFAlO thin film samples slightly increases, accompanied by a few pores, possibly due to the excessive doping of Al [18]. The results suggest that an appropriate amount of Al doping in BFO can accelerate the grain nucleation rate, thereby reducing the grain size and porosity. Fig. 2(e) presents the cross-sectional view of the BFAlO thin film with 0.02 doping, illustrating well-defined columnar grains, layered structure, and a sharp boundary with the ITO substrate. The film's thickness measures around 850 nm.

To comprehensively study the impact of Al doping on the crystal structure of BFO thin films, Raman spectroscopy was performed on the film samples. It is known that the R3c phase of BFO crystals has 13 distinct active Raman vibrational modes, which can be represented by $\int_{RAMAN,R3c} = 4A_1+9E$. These modes are similar to the vibrational modes of rhombohedral R3c perovskites such as $LaMnO_3$ and $LaAlO_3$ [19]. Fig. 3(a)-(e) present the Raman spectra of the BFAlO thin film samples within the test range of 80-700 nm. To further elucidate the characteristics of each vibrational mode, Gaussian components are used to fit the Raman spectra. As shown in Table 1, it is clear that the ferroelectricity of BFO is closely associated with the A modes. After Al doping, changes in the relative intensity and peak width of the Raman modes are observed, primarily due to the random substitution of Fe^{3+} by Al^{3+} at the B-site of the perovskite lattice, leading to structural disorder

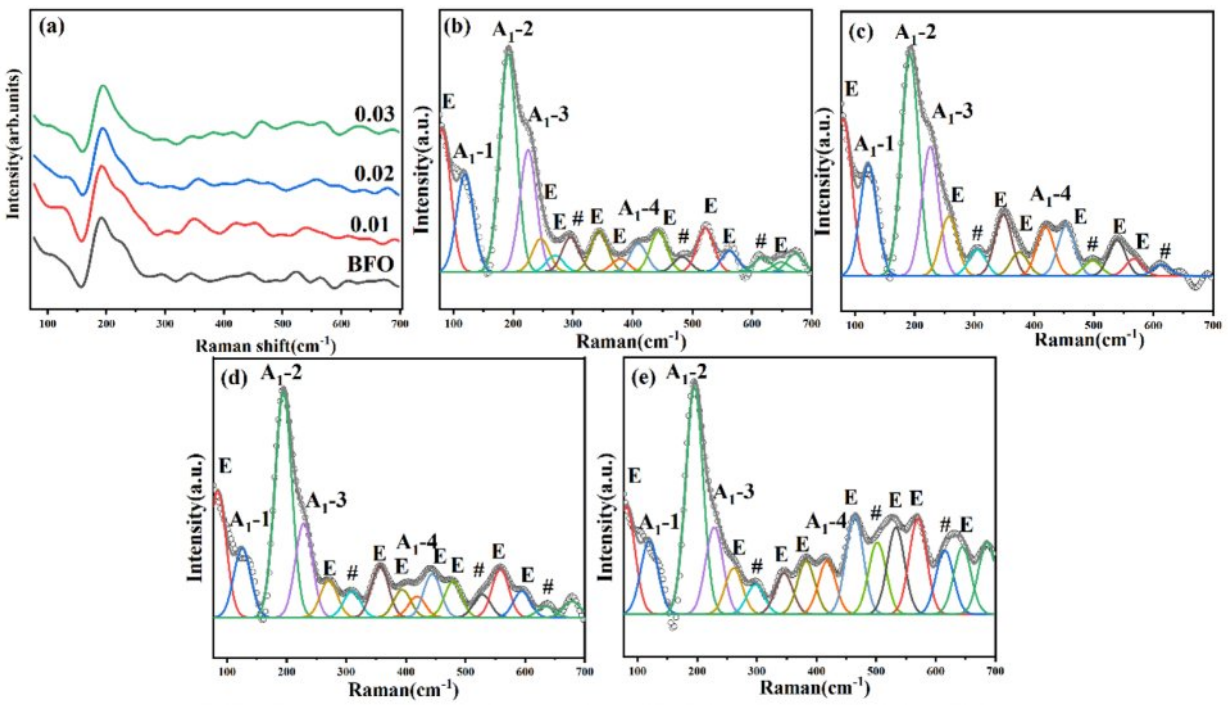

Fig. 3. (a) Raman spectra of the BFAlO thin films with different Al content. Fitting result of the Raman spectra of the (b) BFO, (c) $BF_{0.99}Al_{0.01}O$, (d) $BF_{0.98}Al_{0.02}O$, (e) $BF_{0.97}Al_{0.03}O$ thin film samples.

and lattice distortions caused by size mismatch between ions. Notably, the A_1-1 vibrational mode shifts towards a higher wavenumber (from 118.86 cm^{-1} to 119.81 cm^{-1}) after Al incorporation. The change may be attributed to the lower atomic mass of Al^{3+} (26.98) compared to that of Fe^{3+} (55.84), resulting in distortion of the oxygen octahedra and affecting the state of the Bi-O bonds [20]. In addition, the intensity of the A_1-1 mode is observed to be higher than that of the A_1-2 mode, indicating that the covalent Bi-O bonds and the non-centrosymmetric ferroelectric distortions remain stable in the BFAlO thin films [21]. Moreover, the Raman spectra of all film samples exhibit pronounced peak vibrations at 300, 500, and 620 nm (marked with "#"), which correspond to the characteristics of the orthorhombic Pnma phase in BFO thin films [22-24]. This implies that the BFAlO films

Table 1. Raman modes of BFO films with different Al content.

Raman mode	Raman shift (cm^{-1})			
	BFO	0.01	0.02	0.03
E	80.434	80.327	84.35	81.117
A_1-1	118.86	122.47	125.56	119.81
A_1-2	191.39	192.2	194.53	195.33
A_1-3	224.71	226.05	228.88	228.64
E	246.09	257.08	270.69	261.31
Pnma	295.91	304.86	309.56	297.68
E	343.87	348.46	356.62	345.46
E	379.07	375.54	393.89	382.57
A_1-4	409.73	418.93	418.4	417.78
E	443.53	445.87	443.99	463.97
Pnma	483.03	498.4	478.96	502.04
E	522.01	539.11	527.61	533.21
E	562.02	567.62	558.3	570.03
Pnma	617.98	614.06	594.3	614.65
E	648.98	-	634.12	644.65

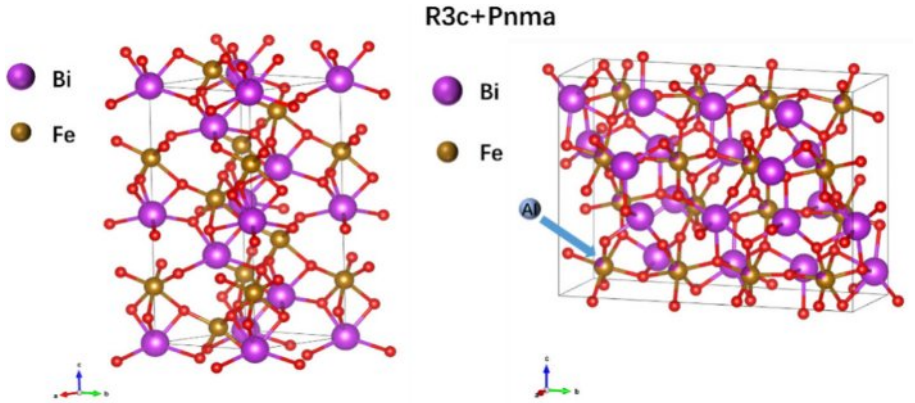

Fig. 4. Schematic diagram of the crystal structure (R3c+Pnma) of the BFAlO thin films.

contain not only the primary R3c phase but also a Pnma phase, as depicted in Fig. 4.

To better comprehend how the valence changes of chemical elements affect the properties of the BFAlO thin films, XPS analysis is performed on all samples. The study reveals that the valence state variation of Fe^{3+} directly affects the oxygen vacancy content, which in turn correlates with the leakage current of the films. Fe *2p* orbital fitting analysis is performed on the BFAlO thin film samples with different doping levels, with results shown in Fig. 5(a)-(d). The characteristic peaks of the Fe-O bond are primarily concentrated around 710.1 eV and 723.2 eV, corresponding to Fe $2p_{3/2}$ and Fe $2p_{1/2}$, respectively [25]. Based on the principles of defect chemistry, there is a direct proportional relationship between the concentration of Fe^{3+} and oxygen vacancies. Fitting analysis of the XPS spectra yields the Fe^{3+}:Fe^{2+} area ratio for the BFAlO film samples as 2.93, 3.14, 3.41, and 3.32, respectively. With increasing Al doping, the concentration of Fe^{3+} initially shows an increasing trend, followed by a slight decrease. The findings indicate that optimal Al doping can inhibit the reduction

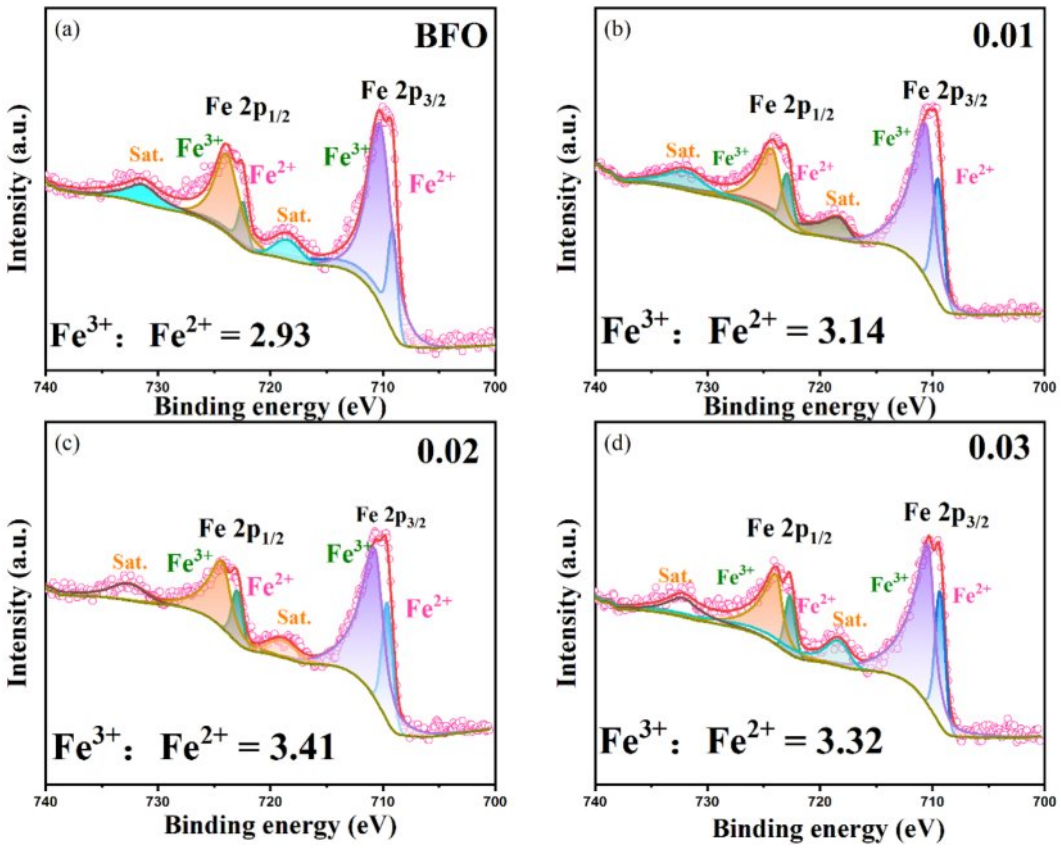

Fig. 5. Fe*2p* orbital XPS fitting of BFAlO films with different Al content: (a) BFO, (b) $BF_{0.99}Al_{0.01}O$, (c) $BF_{0.98}Al_{0.02}O$, (d) $BF_{0.97}Al_{0.03}O$.

of Fe^{3+} to Fe^{2+}, thus decreasing the oxygen vacancy concentration in the films. The reduction in oxygen vacancy concentration can effectively lower the leakage current density and enhance the ferroelectric properties of the films.

$$2Fe_{Fe}^{X} + O_{O}^{X} \rightarrow 2Fe'_{Fe} + V_{O}^{\cdot\cdot} + \frac{1}{2}O_2 \uparrow \quad (2)$$

Fig. 6(a)-(d) show the XPS narrow-scan spectra of the O*1s* orbital peaks for the BFAlO thin films with different Al doping levels. To analyze the O*1s* spectra more accurately, Gaussian-Lorentzian curve fitting is applied to the O*1s* orbital peaks, focusing on the deconvolution of peaks around the binding energy of 529 eV to 531 eV. The O*1s* is decomposed into three main peaks, corresponding to lattice oxygen (O_L), oxygen vacancies (O_V), and adsorbed oxygen (O_A). The spectra reveal that the oxygen vacancies and lattice oxygen atoms occupy a significant area ratio within the O*1s* orbital peak. The relative area ratios of O_V:O_L are calculated, yielding values of 0.36, 0.34, 0.27, and 0.30, respectively. The analysis indicates that with increasing Al doping, the oxygen vacancy concentration in the BFAlO thin films shows a trend of initially decreasing and then increasing. An optimal amount of Al doping can effectively reduce the oxygen vacancy content in the BFAlO thin films, a result that is consistent with previous analyses of the Fe *2p* XPS spectra. The reduction in the oxygen vacancies is typically directly related to the improvement of the film's electrical properties.

Fig. 7(a) exhibits the ferroelectric performance (P-E) hysteresis loops of BFAlO thin film samples with varying Al doping contents, measured under an electric field strength of 640 kV/cm at a frequency of 1 kHz. All the BFAlO thin film samples exhibit asymmetric coercive fields, mainly due to the built-in electric field resulting from uneven charge distribution linked to the disparity between the top and bottom electrodes. As the Al doping level increases from 0 to 0.03, the remnant polarization strength (2Pr) values is 69.54, 88.48, 132.94, and 104.24 μC/cm², respectively, while the corresponding coercive field strength (2Ec) is 703.48, 721.90, 690.52, and 704.26 kV/cm. The results show that the remnant polarization strength initially rises and subsequently falls with increasing Al doping. Fig. 7(b) shows the variation curves of 2Pr and 2Ec with different Al doping levels. At a doping level of 0.02, the BFAlO thin film exhibits a higher remnant polarization strength and a relatively lower coercive field strength, demonstrating better ferroelectric performance. The improvement in ferroelectric performance may

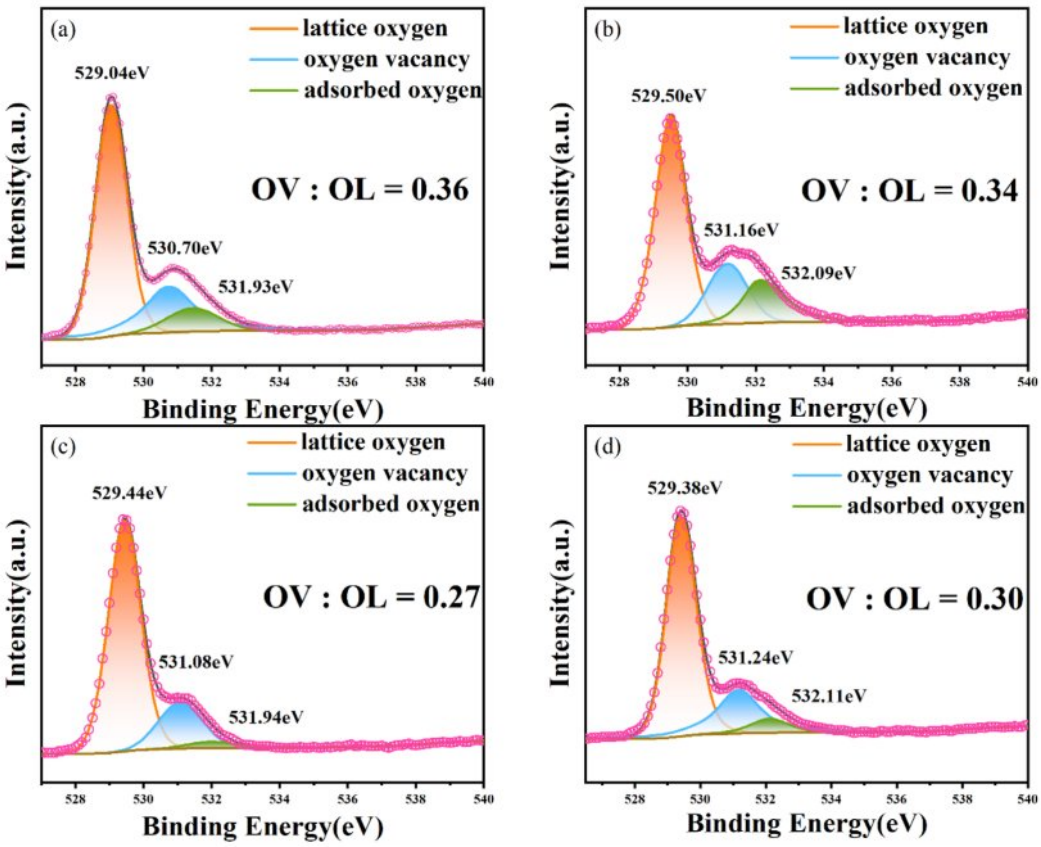

Fig. 6. XPS narrow-sweep O*1s* orbital peak spectra of the BFAlO films with different Al content, (a) BFO, (b) $BF_{0.99}Al_{0.01}O$, (c) $BF_{0.98}Al_{0.02}O$, (d) $BFAl_{0.03}O$.

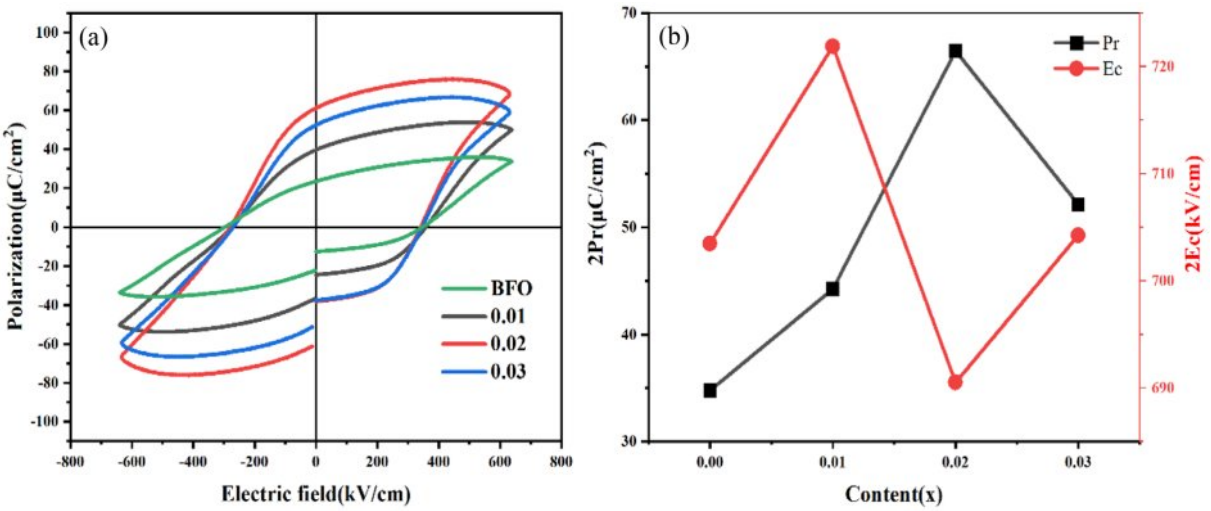

Fig. 7. (a) Hysteresis curves, (b) changes of 2Pr and 2Ec with the Al doping level of the BFAlO thin films.

be the result of the following synergistic effect: (1) The existence of the non-polar Pnma phase, which is a centrosymmetric space group exhibiting paraelectric rather than ferroelectric properties, can reduce the ferroelectric performance of the film samples [14]. (2) The BFAlO thin film sample with a doping level of 0.02 has a lower oxygen vacancy content, which is also beneficial for enhancing ferroelectric performance [25]. The lower oxygen vacancy concentration means that there are fewer defective dipoles $[(\mathbf{Fe}^{2+}_{Fe^{3+}})' - (\mathbf{V}_{O^{2-}})^{\bullet\bullet}]$, which can pin the motion of the domain wall and inhibit the switching of ferroelectric domains, which influences the ferroelectric properties of the films [26-28]. (3) The BFAlO thin film sample with a doping level of 0.02 possesses smaller grains, longer grain boundaries, which improves its breakdown resistance [12].

To examine the impact of Al doping on the optical absorption of the BFAlO thin films, UV-vis absorption spectroscopy is performed on all samples, as depicted in Fig. 8. It is evident that the absorption spectrum of all BFAlO thin film samples exhibit similar characteristics, with the absorption coefficient (α) showing a higher peak below 480 nm, consistent with the typical absorption spectrum of BFO. The doped film samples demonstrate a broadened absorption range and a slight redshift in the absorption peak, indicating that Al doping affects the visible light absorption capability of BFO thin films. The bandgap widths of the BFAlO films are observed to be 2.26 eV, 2.28 eV, 2.34 eV, and 2.31 eV, respectively, showing a slight increasing trend with the addition of Al doping.

Fig. 9 displays the hysteresis loops of the BFAlO thin films pre and post 75 days of aging under an electric field of 640 kV/cm, showcasing that all P-E curves retain excellent rectangularity. It can be observed that all P-E curves maintain good rectangularity. After 75 days of natural aging, the remanent polarization of the BFAlO thin films exhibit varying degrees of reduction. Specifically, the reduction in 2Pr is 24.5%, 22.4%, 16.8%, and 18.7%, respectively, indicating that all BFAlO film samples

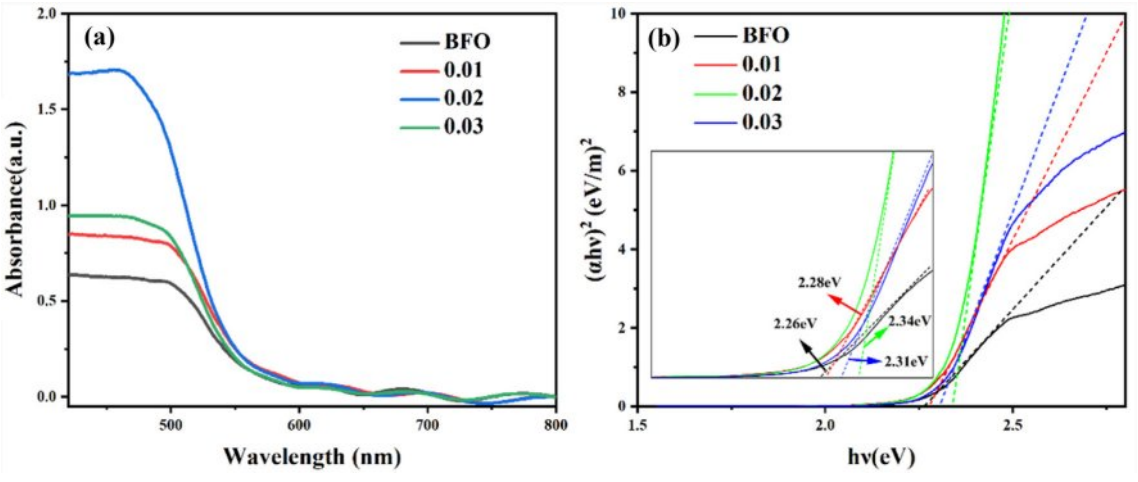

Fig. 8. (a) UV-vis absorption spectra, (b) Tauc curves of the BFAlO thin films with different Al doping level.

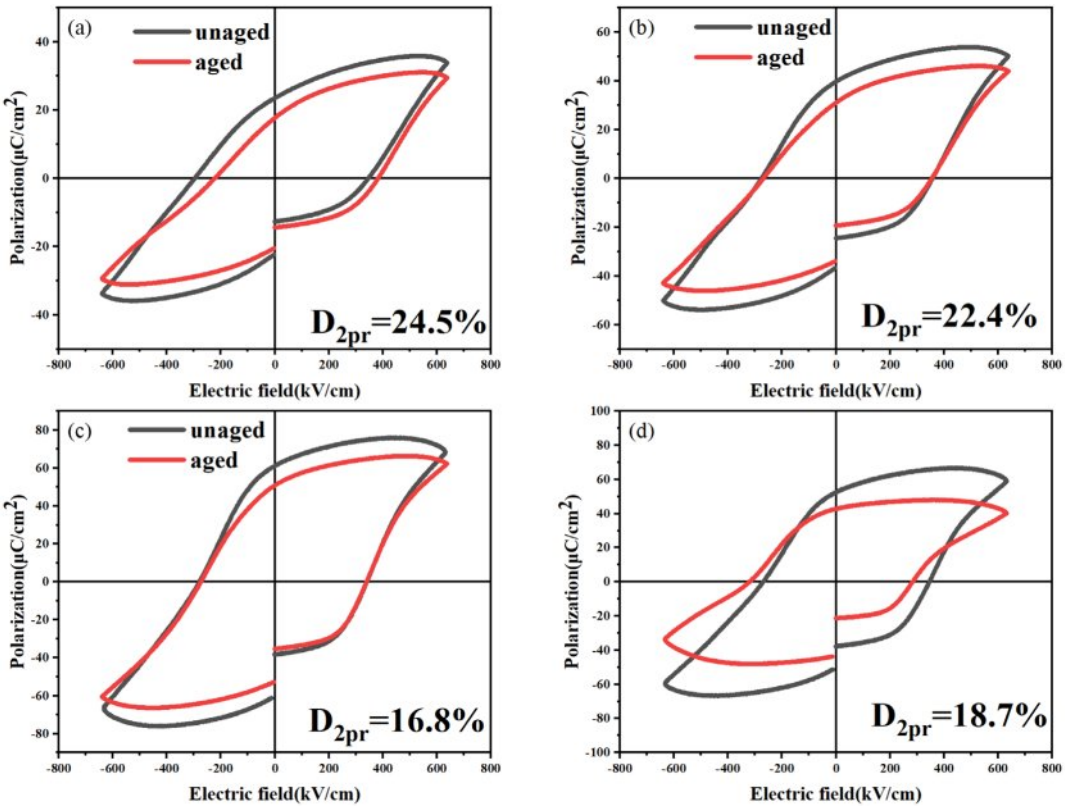

Fig. 9. Aging diagrams of the BFAlO films with different Al content (a) BFO, (b) $BF_{0.99}Al_{0.01}O$, (c) $BF_{0.98}Al_{0.02}O$, (d) $BF_{0.97}Al_{0.03}O$.

undergo different extents of performance degradation. The film sample with a doping level of 0.02 shows a relatively minor decrease in ferroelectric performance, demonstrating better ferroelectric stability. This could be due to the reduced number of oxygen vacancies in the sample, resulting in fewer defect dipoles. Defect dipoles can increase the pinning effect on ferroelectric domains, hindering domain switching and thus accelerating the aging of the sample [29]. Therefore, the decrease in defect dipoles not only facilitates domain switching but also helps to delay the aging process of the sample.

To elucidate the intrinsic principles of the aging mechanism more clearly, an in-depth discussion on the internal connection between the distribution of oxygen vacancies and the domain structure in BFAlO thin films is conducted. Fig. 10(a) shows a projection on the ab plane, from which the distribution of oxygen vacancies can be observed. In the unaged film samples, the oxygen vacancy distribution adheres to cubic symmetry principles ($P_1^{Vo} = P_2^{Vo} = P_3^{Vo} = P_4^{Vo}$) [31-33]. However, such a distribution may lead to a mismatch in crystal structure symmetry and that of defects, which significantly impacts the domain structure and the domain switching process. The symbol P_n^{Vo} (n=1-4) represents the probability of the presence of oxygen ions at sites. As shown in Fig. 10(b), the fresh film samples exhibit a certain degree of instability, which may be caused by the uneven oxygen vacancy distribution. To achieve a more stable state, the samples follow the principle of symmetry coordination short-range order (SC-SRO), achieving a stable state $P_1^{Vo} = P_2^{Vo} > P_3^{Vo} = P_4^{Vo}$ through short-range migration of oxygen vacancies. According to the symmetrically coordinated short-range order (SC-SRO) principle, this state is unstable. However, the thermodynamic driving force provided by the SC-SRO principle makes the defect symmetry and crystal symmetry converge, and at the same time drives the migration of oxygen vacancy $(\mathbf{V_O}^{2-})^{\bullet\bullet}$, lead to $[(\mathbf{Fe}^{2+}_{\mathbf{Fe}^{3+}})' - (\mathbf{V_O}^{2-})^{\bullet\bullet}]$ defects such as dipole short-range orderly distribution and formation of the internal electric field in P_D [34]. After the removal of the applied electric field E, the unchanged defect symmetry and related P_D provide a restorative force to restore the changed P_S to its original direction, and the ordered defect dipole drives domain switching in the doped ferroelectric body; thus, the aging phenomenon of the BFAlO films is observed [35].

During the short-range migration of oxygen vacancies, pinning centers may form at the domain walls. These pinning centers hinder domain wall motion, adversely affecting the reversible switching process of domains. The impeded movement of domain walls makes domain switching difficult, which negatively impacts the ferroelectric properties of the material. When the doping level is 0.02, the BFAlO thin film sample exhibits better ferroelectric stability, which is closely related to the decreased content of oxygen vacancies.

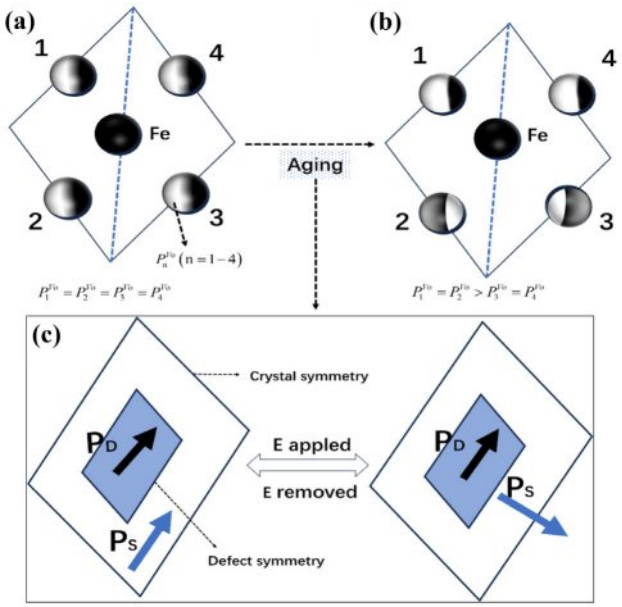

Fig. 10. Crystal structure symmetry and defect symmetry of the BFAlO films with different Al content: (a) fresh films, (b)-(c) aged films [30].

A lower concentration of oxygen vacancies means fewer pinning centers encountered during domain wall movement, which enhances the migration of domain walls and consequently benefits the reversible switching of domains [30]. This data is consistent with XPS results, further confirming the significant impact of oxygen vacancy content on domain wall movement and domain switching. Therefore, an appropriate amount of Al doping in BFO can effectively reduce the oxygen vacancy concentration in the BFAlO thin films, thereby enhancing the mobility of domain walls and providing more driving force for reversible domain switching. This not only helps to improve the ferroelectric property of the BFAlO thin films but also enhances their resistance to aging.

Conclusion

$BiFe_{1-x}Al_xO_3$ ferroelectric thin films with varying levels of Al doping were fabricated on ITO/glass substrates using the sol-gel method to explore the influence of Al doping on both the structural and functional attributes of the BFAlO films. This study also aimed to delve into how Al doping impacts the aging mechanism of these films. The findings reveal that all BFAlO samples exhibit a composition of Pnma and R3c phases. The introduction of Al into BFO leads to the formation of finer grains and enhances the densification of the films. X-ray photoelectron spectroscopy (XPS) analysis indicates that at a doping level of 0.02, the BFAlO thin film samples display relatively low oxygen vacancy content and reduced Fe^{2+} concentration. This effectively suppresses the valence fluctuations of Fe ions, thereby diminishing the number of domain wall pinning centers encountered during domain wall migration. Consequently, this boosts the mobility of domain walls, facilitating easier domain switching and thus decelerating the film's aging process. The BFAlO thin film sample doped with 0.02 exhibits a significant remnant polarization strength ($2Pr$ = 132.94 $\mu C/cm^2$) and a low coercive field strength ($2Ec$ = 690.52 kV/cm). Following a 75-day aging period, the remnant polarization strength of the BFAlO films experiences reduction of 24.5%, 22.4%, 16.8%, and 18.7%, respectively.

Acknowledgments

Thanks to Jining No.1 People's Hospital lab for the Raman spectra testing.

References

1. G.M. Bak, C.G. Song, and J.W. Yoon, J. Ceram. Process. Res. 19[3] (2018) 253-256.
2. I.A. Salmani, M.S. Khan, J. Ali, A.K. Hafiz, M. Mehkoom, S.M. Afzal, and M.S. Khan, Phys. Rev. B Condens. Matter. 55 (2023) 414750.
3. D. Sando, F. Appert, Bin Xu, O. Paull, S.R. Burns, C. Carrétéro, B. Dupé, V. Garcia, Y. Gallais, A. Sacuto, M. Cazayous, B. Dkhil, J.M. Le Breton, A. Barthélémy, M. Bibes, L. Bellaiche, V. Nagarajan, and J. Juraszek, J. Appl. Phys. Rev. 6[4] (2019) 041404.
4. A. Raj, M. Kumar, A. Kumar, K. Singh, S. Sharma, R.C. Singh, M.S. Pawar, M.Z.A. Yahya, and A. Anshul, Ceram. Int. 49[1] (2023) 1317-1327.
5. H.Y. Liu, L.X. Wang, Z.B. Ma, X.D. Guo, B.D. Yao, Y.Y. Wang, Y. Liu, F.Q. Zhang, and L.Y. Zhu, J. Alloys Compd. 918 (2022) 165628.
6. F. Mumtaz, G.H. Jaffari, and S.I. Shah, Phys. Rev. B Condens. Matter. 664 (2023) 414993.
7. Z.B. Ma, H.Y. Liu, L.X. Wang, B.D. Yao, Y.Y. Wang, Y. Liu, F.Q. Zhang, W.W. Qin, and J. Xu, J. Mater Chem. 9[41] (2021) 14659-14668.
8. J.X. He, J.W. Wang, Y. Liu , Y. Liu , Z.Jiang, S.H. Sun, Z.F. Jing, and F.Q. Zhang, J. Mater. Sci-Mater. El. 35[4] (2024) 304.
9. A. Wrzesińska, A. Khort, M. Witkowski, J. Szczytko, J. Ryl, J. Gurgul, D.S. Kharitonov, K. Łątka, T. Szumiata, and A. Wypych Puszkarz, Sci. Rep. 11[1] (2021) 22746.
10. N.M.A. Zulkafli, M.K. Yaakob, M.H. Ridzwan, M.F. Kasim, M.M. Mahat, R. Rajmi, M.H. Mamat, A.A. Mohamad, and M.Z.A. Yahya, Physica B: Condens. Matter. 648 (2023) 414417.
11. P.V. Kanjariya, B Mater Sci. 46[4] (2023) 188.
12. Y.Y. Wang, J.T. Tang, Y. Liu, B.D. Yao, J.X. He, F.Q. Zhang, and W.W. Qin, Mater. Sci. Semicond. Process. 155 (2023) 107236.
13. A.K. Vishwakarma, P. Tripathi, A. Srivastava, A.S.K. Sinha, and O.N. Srivastava, Int. J. Hydrogen Energy. 42[36] (2017) 22677-22686.
14. Z.B. Ma, H.Y. Liu, L.X. Wang, F.Q. Zhang, L.Y. Zhu, and S.H. Fan, J. Mater. Chem C. 8[48] (2020) 17307-17317.
15. X.L. Liang, J.Q. Dai, C.C. Zhang, and T.F. Cao, J. Sol-Gel Sci. Technol. 98[1] (2021) 45-53.

16. V. Verma, J. Alloys Compd. 641 (2015) 205-209.
17. S. Chandel, P. Thakur, M. Tomar, V. Gupta, and A. Thakur, Ceram. Int. 43[16] (2017) 13750-13758.
18. T.F. Cao, J.Q. Dai, and X.W. Wang, Ceram. Int. 46[6] (2020) 7954-7960.
19. M.V. Abrashev, A.P. Litvinchuk, M.N. Iliev, R.L. Meng, V.N. Popov, V.G. Ivanov, R.A. Chakalov, and C. Thomsen, Phys. Rev. B. 59[6] (1999) 4146-4153.
20. S.S. Chandel, P. Thakur, S.S. Thaku, V. Kanwar, M. Tomar, V. Gupta, and A Thakur, Ceram. Int. 44[5] (2018) 4711-4718.
21. P.C. Sati, M. Kumar, S. Chhoker, and M. Jewariya, Ceram. Int. 41[2] (2015) 2389-2398.
22. F. Mumtaz, G.H. Jaffari, G.S. Khan, and A. Ali, Thin. Solid. Films. 789[30] (2024) 140175.
23. J. Bielecki, P. Svedlindh, D.T. Tibebu, S.Z. Cai, S. Eriksson, L. Börjesson, and C.S. Knee, Phys. Rev. B. 86[18] (2012) 184422.
24. C. Gumiel, T. Jardiel, D.G. Calatayud, T. Vranken, M.K. Bael, A. Hardy, M.L. Calzada, R. Jiménez, M. García-Hernández, F.J. Mompeán, A.C. Caballero, and M. Peiteado, J. Mater. Chem. C. 8[12] (2020) 4234-4245.
25. C.C. Zhang, J.Q. Dai, and X.L. Liang, Ceram. Int. 47[12] (2021) 16776-16785.
26. F.Q. Zhang, S.H. Fan, C.J. Wang, X.B. Xie, and X.D. Guo, J. Ceram. Process. Res. 18[4] (2017) 301-304.
27. L.X. Wang, H.Y. Liu, L.Q. Liu, and F.Q. Zhang, J. Ceram. Process. Res. 22 (2021) 121-129.
28. Y. Liu, Z.B. Ma, Z. Jiang, J.X. He, S.H. Sun, Z.F. Jing, and F.Q. Zhang, J. Mater. Sci-Mater. El. 35 (2024) 1204.
29. Y. Liu, Z.B. Ma, Y.Y. Wang, B.D. Yao, J.X. He, J. Li, and F.Q. Zhang, Ceram. Int. 48 (2022) 28112-28120.
30. Z.Y. Feng and X.B. Ren, Phys. Rev. B. 77[13] (2008) 134115.
31. X.B. Ren, Nat. Mater. 3[2] (2004) 91-94.
32. X.B. Ren and K. Otsuka, Phys. Rev. Lett. 85[5] (2000) 1016-1019.
33. L.X. Zhang and X.B. Ren, Phys. Rev. B. 3[9] (2006) 094121.
34. Y.Y. Guo, Y. Zhao, H.G. Zhang, and N. Zhang, J. Alloys. Compd. 696 (2017) 814-819.
35. Z.L. Zhu, L.H. Luo, F.F. Wang, P. Du, X.T. Zhou, Q. Zhang, W.P. Li, and Y.J. Wang, J. Eur. Ceram. 40[3] (2020) 689-698.